Efficient terahertz spin-to-charge current conversion in IrAl compounds 🔵EP

Junwei Tong 🆔 ; Peng Wang; Hongsong Qiu 🆔 ; Tom S. Seifert 🆔 ; Ilya Kostanovski 🆔 ; Stuart S. P. Parkin 🆔 ; Tobias Kampfrath 🆔 ; Oliver Gueckstock ✉ 🆔

Check for updates

View Online Export Citation

Articles You May Be Interested In

Stability of metallic CsCl-structured alloys under ion irradiation

J. Appl. Phys. (June 1986)

Spintronic sources of ultrashort terahertz electromagnetic pulses

Appl. Phys. Lett. (May 2022)

Rotating spintronic terahertz emitter optimized for microjoule pump-pulse energies and megahertz repetition rates

Appl. Phys. Lett. (August 2024)
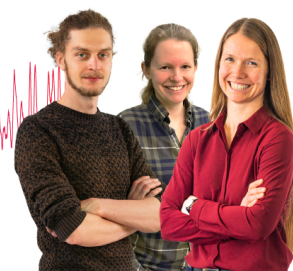
Efficient terahertz spin-to-charge current conversion in IrAl compounds (EP)

View Online   Export Citation   CrossMark

Junwei Tong,[1] (iD) Peng Wang,[2,3] Hongsong Qiu,[1,4] (iD) Tom S. Seifert,[1] (iD) Ilya Kostanovski,[2] (iD) Stuart S. P. Parkin,[2,3] (iD)
Tobias Kampfrath,[1] (iD) and Oliver Gueckstock[1,a)] (iD)

AFFILIATIONS

[1]Freie Universität Berlin, Department of Physics, 14195 Berlin, Germany
[2]Max Planck Institute of Microstructure Physics, 06120 Halle, Germany
[3]Institute of Physics, Martin Luther University Halle-Wittenberg, 06120 Halle, Germany
[4]State Key Laboratory of Spintronics Devices and Technologies, School of Integrated Circuits, Nanjing University, Suzhou, China

[a)]Author to whom correspondence should be addressed: oliver.gueckstock@fu-berlin.de

ABSTRACT

The interconversion between spin and charge currents is vital for developing spintronics technologies, which require materials with high spin-to-charge-current conversion efficiency (SCC). The alloy IrAl was shown to exhibit a large spin Hall angle at gigahertz frequencies. Here, we use spintronic terahertz emission spectroscopy to investigate terahertz SCC in Ir_xAl_{1-x}|FM heterostructures with a ferromagnetic layer FM of CoFeB and Ni as a function of the composition ratio x. We observe a strongly x-dependent terahertz-signal amplitude, whereas no change in the dynamics of the ultrafast in-plane charge current is seen. For $x = 0.48$, we find that the SCC efficiency in Ir_xAl_{1-x} reaches up to 65% of that of Pt. Signals from Ir_xAl_{1-x}|Ni suggest that orbital contributions to the signal are minor. This study highlights the potential of IrAl alloys for SCC in ultrafast spintronic applications.

The conversion between spin and charge currents is pivotal for advancing spintronics.[1–3] Therefore, the identification of materials with highly efficient spin-to-charge conversion (SCC) is crucial. In metals, a variety of SCC mechanisms is known, such as the inverse spin Hall effect (ISHE)[1] and the inverse spin Rashba–Edelstein effect (ISREE).[4–6] Most commonly, transition metals with large spin–orbit coupling, e.g., Pt and W, are employed for efficient SCC.[1,7–9] Other material classes that are predicted to potentially offer large SCC efficiencies are, e.g., topological insulators due to the spin-momentum locking of their topological surface states.[1,2,7]

Recently, a giant spin Hall angle was observed in binary transition-metal-aluminum alloys, like IrAl, and attributed to (extrinsic) defect-mediated scattering, thereby providing an efficient way to control the magnetization by spin–orbit torques.[10] However, the SCC efficiency in these alloys has not yet been addressed at the femtosecond time scale, which is the native time scale of many spintronic processes.[11] To this end, terahertz emission spectroscopy (TES) combines spin transport and SCC[12,13] at terahertz (THz) frequencies with large sample throughput, thereby providing insight that are important for the development of high-speed spintronic applications.

Here, we investigate SCC in Ir_xAl_{1-x}|CoFeB heterostructures with varying stoichiometry using TES. We observe a strongly composition-dependent THz-emission amplitude. By accounting for the THz impedance and pump-pulse absorptance of each sample, we identify a high SCC efficiency in Ir_xAl_{1-x}, reaching up to 65% of Pt when the Ir content is $x = 0.48$. A detailed analysis of amplitude and dynamics of the optically induced in-plane charge current rules out a significant contribution of orbital-to-charge conversion in IrAl compounds.

Figure 1 shows a schematic of our THz-emission experiment. We use femtosecond laser pulses (nominal pulse duration of 10 fs, central wavelength of 800 nm, pulse repetition rate of 80 MHz, and pulse energy of 2 nJ) to optically excite a FM|NM stack consisting of a ferromagnetic-metal layer (FM) of CoFeB(5 nm) or Ni(5 nm) and a non-ferromagnetic metal layer NM of Ir_xAl_{1-x}(5 nm) or Pt(5 nm). The pump pulse increases the electronic temperature of FM, thereby inducing a transient excess of magnetization (spin voltage) inside the FM. To release the spin voltage, the FM demagnetizes by (i) local transfer of spin angular momentum to the crystal lattice and/or (ii) injects a spin current with density $j_s(t)$ into the adjacent NM.[14] In the
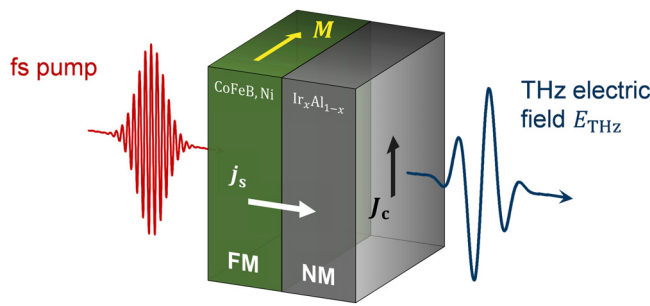
FIG. 1. Schematic of the experiment. A femtosecond laser pulse excites a FM|NM stack and launches a spin current from the ferromagnetic metal layer (FM) of CoFeB or Ni to an adjacent non-magnetic metal layer NM of Ir_xAl_{1-x} or Pt. In NM, the spin current (density j_s) is converted into a transverse charge current (sheet density J_c) that emits a THz electromagnetic pulse. The THz electric field is detected by electro-optic sampling. The FM magnetization M is saturated by an external in-plane magnetic field.

NM, $j_s(t)$ is converted into a transverse charge current with sheet density $J_c(t)$ by SCC, which includes such processes as the inverse spin Hall effect and the inverse Rashba Edelstein effect. The time dependence of $J_c(t)$ results in the emission of an electromagnetic pulse with frequencies extending into the THz range.[12]

To detect the emitted THz electric field $E(t)$, we make use of electro-optic sampling in a 250 μm-thick GaP(110) crystal,[13] resulting in signals $S(t, \pm M)$ vs time t (see Fig. S1). Here, the sample magnetization M is set by an external in-plane magnetic field with magnitude 70 and 370 mT for CoFeB and Ni, respectively. As we are interested in effects odd in M, we focus on the signal $S_-(t) = [S(t, +M) - S(t, -M)]/2$. All measurements are performed in a dry-air atmosphere if not explicitly noted otherwise. To retrieve the THz electric field $E(t)$ from the THz signal $S_-(t)$, we use $\tilde{S}(\omega) = \tilde{H}(\omega)\tilde{E}(\omega)$ in the frequency domain with $\tilde{H}(\omega)$ denoting the setup-specific transfer function accounting for frequency-dependent propagation of $\tilde{E}(\omega)$ and the detector response function. More details on this retrieval procedure can be found in Ref. 15.

The films were deposited in an AJA 'Flagship Series' sputtering system in the presence of Ar gas on 10×10 mm^2 MgO substrates with [001] orientation. The base pressure before deposition was less than 10^{-8} Torr, while the pressure during deposition was 3 mTorr. The Ir_xAl_{1-x} alloy thin films were prepared by co-sputtering from individual iridium and aluminum targets with 2-in. diameter and 0.25-in. thickness, and the ratio of x is varied by tuning the applied sputtering power to the Ir target. The applied sputtering power to the Ir target changed from 15 to 125 W with fixed applied sputtering power to the Al target of 95 W. The CoFeB, Pt, and Ni layers were prepared by sputtering from a single target with nominal composition of $Co_{20}Fe_{60}B_{20}$, Pt, and Ni (99.99%), respectively. The capping layer of MgO is grown by off-axis radio frequency (RF) sputtering.

High-resolution x-ray diffraction (XRD) measurements were performed using a Bruker D8 Discover system with Cu-$K\alpha_1$ radiation ($\lambda = 1.54$ Å) at room temperature. The composition of the thin-film samples is calibrated by nondestructive Rutherford Backscattering spectroscopy with an accuracy of ~1–2 at. %. To quantify the amount of energy deposited in each sample, we additionally measure the pump-light absorptance A, which can be obtained from the reflected and transmitted pump power through the sample.[16]

To determine the outcoupling of the THz electric field $E(t)$ from the metallic thin film, we perform THz-transmission measurements on all samples with an optimized spintronic THz emitter on a Si substrate [TeraSpinTec GmbH] to generate broadband THz pulses.[17] The latter are transmitted through the bare substrate and substrate including the sample. Figure 2(c) shows an example ($x = 0.48$) of the transmitted THz field through the MgO substrate $\tilde{S}_{sub}(\omega)$ and Ir_xAl_{1-x}|CoFeB sample $\tilde{S}_{sam}(\omega)$. All raw data THz transmission waveforms are shown in Fig. S5. From the THz transmittance $\tilde{t}(\omega) = \tilde{S}_{sam}(\omega)/\tilde{S}_{sub}(\omega)$, we obtain access to the frequency-dependent impedance $Z(\omega)$ by $Z(\omega) = \tilde{t}(\omega)Z_0/(n_1 + n_2)$, which is directly proportional to the outcoupling of $E(t)$ from the sample. The details can be found in the supplementary material and in Ref. 18.

Figure 2(a) shows typical THz-emission raw data signals $S_-(t)$ from Ir_xAl_{1-x}|CoFeB stacks with different Ir content x. All $S_-(t)$ exhibit very similar dynamics. This observation suggests that the temporal dynamics of the spin-current driving force, the spin current propagation, and the SCC do not change substantially as a function of x, consistent with previous reports on AuPt and CoFe.[19,20]

Remarkably, however, the amplitude of $S_-(t)$ strongly depends on the Ir_xAl_{1-x} composition parameter x [Fig. 2(a)]. To quantify this behavior, we contract the THz signals to a single amplitude value by taking the peak-to-peak value, as summarized in Fig. 3(a). We observe a maximum THz amplitude at a composition ratio of $x = 0.48$. We further check if the emitted THz electric field is dependent on the pump polarization to exclude any signal contributions due to other driving forces.[21,22] We observe no difference of the THz waveforms upon variation of the linear pump polarization angle (Fig. S2) and pump helicity (Fig. S3). Figure 2(b) shows the Fourier amplitude spectrum of the THz waveform for $x = 0.48$ from Fig. 2(a). We observe THz emission up to 25 THz, limited by the GaP detection crystal. Note that the dip at 8 THz originates from a phonon of the detection GaP crystal.[23] Spectra for all other compositions of IrAl are shown for completeness in Fig. S4, where we do not observe any significant differences compared to $x = 0.48$, in agreement with the time-domain THz signals $S_-(t)$ in Fig. 2(a).

Figure 2(a) and Fig. 3(a) indicate that the THz signal amplitude is strongly influenced by the IrAl composition. To better understand this behavior, we write down the amplitude of the emitted THz field as expected for the situation of our experiment,

$$E(\omega) \propto \mu_s(\omega)T(\omega) \cdot [\gamma_{ISHE}(\omega)\lambda_s(\omega) + \lambda_{ISREE}(\omega)] \cdot Z(\omega). \quad (1)$$

Here, $E(\omega)$ is the Fourier amplitude of the THz field behind the sample at a frequency of $\omega/2\pi$. The three terms on the right-hand side quantify the (i) spin-current injection from FM to NM, (ii) the SCC in NM, and (iii) the charge-current-to-field conversion. More precisely, (i) $\mu_s(\omega)$ is the spin voltage and $T(\omega)$ is the transmission of the generated spin current across the interface toward NM, (ii) $\gamma_{ISHE}(\omega)$ is the ISHE angle of NM and $\lambda_s(\omega)$ is the relaxation length of the spin current in NM, and (iii) $Z(\omega)$ is the sample impedance. Equation (1) also accounts for SCC by the ISREE through the ISREE strength $\lambda_{ISREE}(\omega) = J_c(\omega)/j_s(\omega)$.

To quantify the impact of x on each factor in Eq. (1), we first determine $Z(\omega)$. Due to the flat frequency response of $Z(\omega)$ (see Fig. S6), we just consider an average over the frequencies from 0.4 to 5 THz for each sample. The impedance Z vs x of all IrAl samples is shown in Fig. 3(b). We see that the impedance is almost constant for
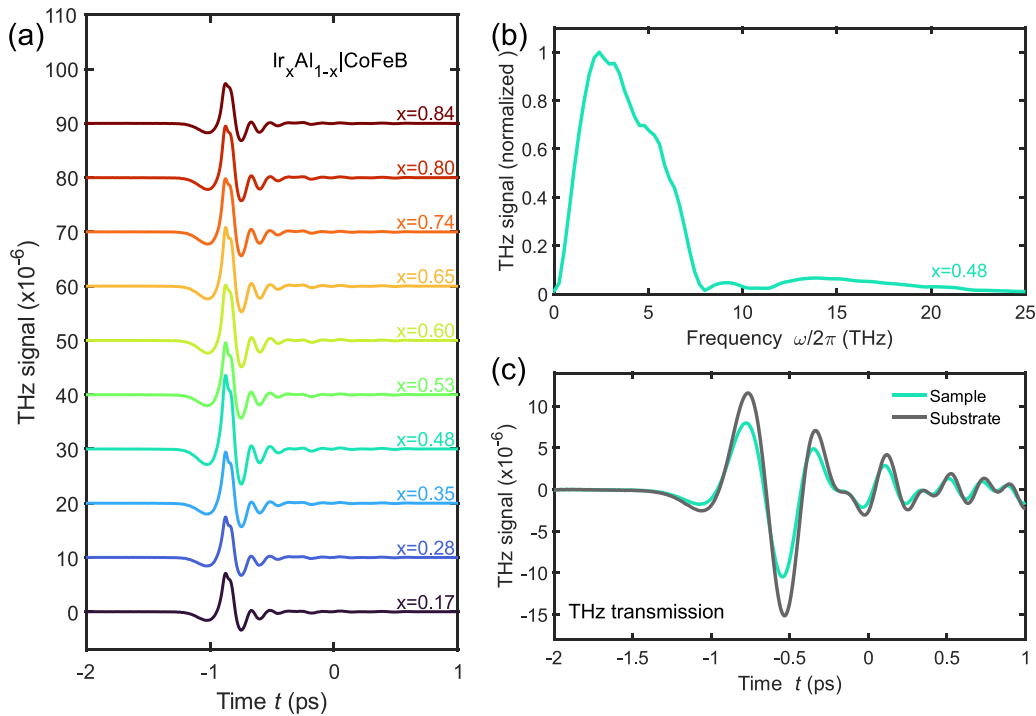
FIG. 2. THz signals from Ir_xAl_{1-x}|CoFeB. (a) THz electro-optic signal $S_-(t)$ odd in M from Ir_xAl_{1-x}|CoFeB for varying composition ratios x. The waveforms are vertically offset for clarity. (b) Fourier amplitude spectrum for $x = 0.48$. (c) THz signals detected following transmission of a THz pulse through $Ir_{48}Al_{52}$|CoFeB sample on a MgO substrate and, for reference, through a bare MgO substrate.

all x, in contrast to the strongly composition-dependent THz amplitude [Fig. 3(a)].

Second, the spin-voltage dynamics is the same in all samples because the signal dynamics is independent of x and of the NM layer (IrAl vs Pt).[14] Therefore, just the amplitude of μ_s may differ with NM and, thus, x. We assume that the spin voltage scales according to $\mu_s \propto A/d$. This assumption is justified because the pump energy is uniformly distributed over the entire FM thickness. Figure 3(c) shows the pump light absorptance A as a function of x, which reflects the thickness mean excitation of the entire sample. A is almost constant over the entire composition range.

With this information, we can determine the effective SCC efficiency $\alpha_{SCC} = T(\omega) \cdot [\gamma_{SH}(\omega)\lambda_s(\omega) + \lambda_{ISREE}(\omega)]$ of IrAl relative to NM = Pt. We find that α_{SCC} [Fig. 3(c)] follows the trend of the THz amplitude [Fig. 3(b)] quite faithfully due to the composition-independent THz impedance and pump absorptance. Here, we assume $\lambda_s(\omega)$ to be mostly independent of x because the transport of spin-polarized electrons is dominated by ballistic transport[24–26] rather than a diffusive motion of electrons. The ballistic transport length is determined by the Drude scattering rate and, thus, the mean free path inside IrAl. On the one hand, the mean free path for Ir and Al is very similar in the range of a few nanometer;[27] on the other hand, our frequency-resolved impedance measurements show a very similar slope over the entire composition range (Fig. S6), which indicates very similar Drude scattering rates. Interestingly, we find that, for $x = 0.48$, the SCC in Ir_xAl_{1-x} is up to 65% of Pt indicating that IrAl is a material for efficient SCC at THz frequencies.

As already indicated in Eq. (1), we consider SCC contributions due to the ISHE and ISREE. As both effects have the same macroscopic symmetry, a clear separation of these two SCC effects is difficult. Nevertheless, both effects may have different charge-current dynamics, as the ISREE requires spin accumulation that may take more time than the ISHE, which is considered to happen instantaneously.[14] Therefore, we consider the charge-current sheet density $J_c(t)$ instead of the THz signals $S_-(t)$. Note that $S_-(t)$ is convoluted with a setup-specific transfer function $H(t)$ that might be misleading for the interpretation of the underlying current dynamics. The obtained $J_c(t)$ are shown in Fig. 4(a) for FM = CoFeB and NM = $Ir_{48}Al_{52}$ and the reference NM = Pt. In Pt, it is reasonable to assume a dominant ISHE, as shown in various studies.[13,14,17,28] We observe no drastic changes in the dynamics of $J_c(t)$ for IrAl vs Pt, indicating a negligible ISREE contribution. The small differences between the two charge currents in Fig. 4(a) occur on time scales that are very close to our time resolution and, thus, insignificant. A previous study showed that SCC in IrAl is dominated by extrinsic contributions to the ISHE,[10] in contrast to the SCC in Pt, which is mainly due to the intrinsic contribution.[8] This finding may also reflect the reason for the quite sizable SCC in IrAl at THz frequencies.

Recently, it was found that orbital currents can also play an important role for the transport of angular momentum and conversion into charge currents by orbital-to-charge conversion (OCC) in FM|NM heterostructures.[29–33] To check if a dominant OCC happens inside IrAl, we compare F = Ni as a good source of orbital currents with FM = CoFeB, which predominantly injects a spin current into
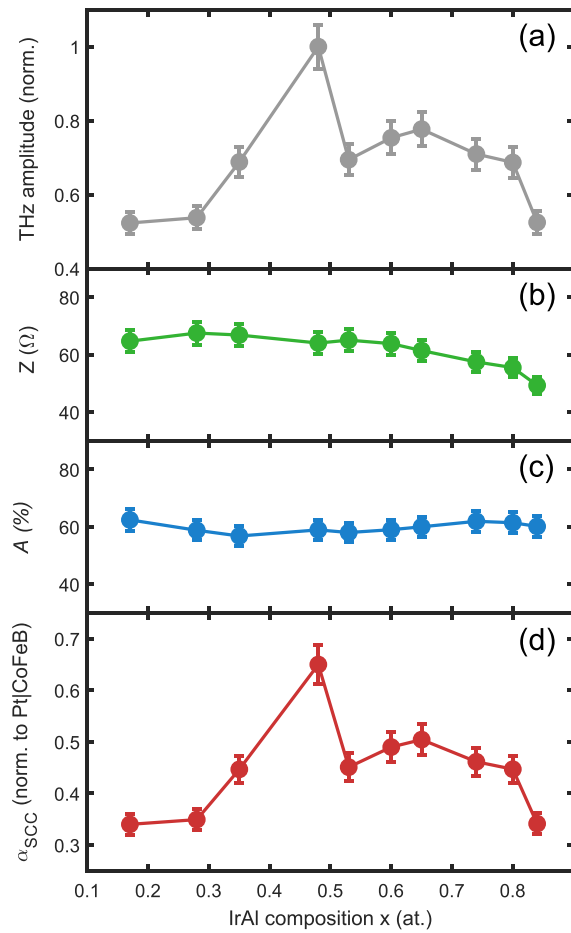
FIG. 3. Spin-to-charge conversion efficiency of Ir_xAl_{1-x}. (a) THz peak-to-peak amplitude normalized by the maximum, (b) frequency-averaged sample impedance Z, (c) pump-pulse absorptance A, and (d) SCC strength α_{SCC} as a function of Ir content x.

FIG. 4. Charge-current dynamics in IrAl and Pt. (a) Charge current sheet density $J_c(t)$ vs time t for CoFeB and (b) Ni as ferromagnetic layer FM. Signals for Pt and IrAl as normal-metal layer NM are normalized by their minimum, multiplied by -1 and rescaled by a factor indicating the SCC efficiency relative to Pt.

IrAl.[32–37] The charge-current sheet density $J_c(t)$ for IrAl|FM and a corresponding reference sample Pt|FM are shown in Fig. 4. For samples with FM = Ni, we find almost identical dynamics as for FM = CoFeB. We extract an SCC/OCC efficiency of 62% relative to Pt [Fig. 4(b)], which is, within the estimated uncertainty of $\approx 6\%$, the same as $\alpha_{SCC} = 64\%$ for CoFeB|IrAl [Fig. 4(a)]. Therefore, any OCC contribution in IrAl is minor compared to SCC. This conclusion includes OCC due to the inverse orbital Rashba–Edelstein effect that may lead to distinctively different dynamics of $J_c(t)$ as concluded in a previous study.[32] The NM = IrAl layers are sufficiently thick such that a potential orbital current with propagation length λ_L,[32] which is larger than the spin-current relaxation length of ~ 1 nm,[14] would be already broadened by dispersion of the injected orbital current inside the 5-nm-thick NM layer. They would, thus, lead to a modified dynamics of $J_c(t)$ (Fig. S7), which is not observed, consistent with the conclusion that orbital contributions are minor in IrAl.

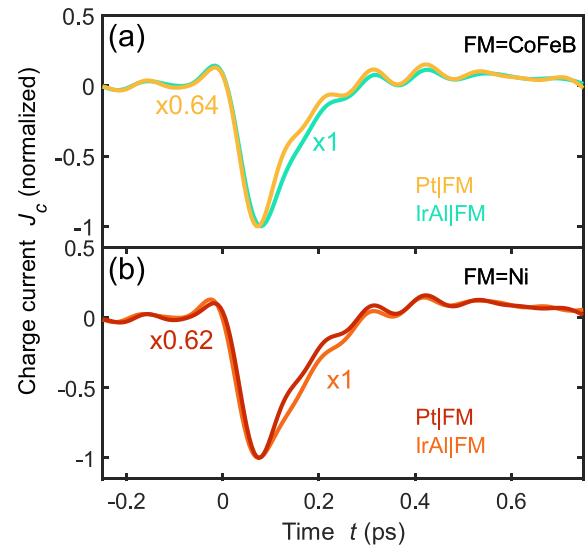Finally, we compare our results with a previous study of the SCC in Ir_xAl_{1-x}[10] at GHz frequencies. This study shows a strong dependence of the SCC on the composition x, the trend of which qualitatively agrees with our results. Quantitatively, the maximum SCC was found around $x = 0.30$, where the crystal structure undergoes a change from a poorly to higly crystalline phase. In contrast, we observe a maximum at $x = 0.48$. This discrepancy may be due to (i) a different calibration during the co-sputtering process of Ir and Al and, thus, a varying composition x compared to the samples used in Ref. 10. (ii) The different methods for measuring SCC may exhibit different sensitivities with respect to the IrAl bulk and IrAl/FM interface.

With regard to (ii), we note that spintronic THz emission is a highly sensitive probe of the NM/FM interface,[15,18,38] likely more sensitive than methods operating at GHz frequencies, in particular because spin-current relaxation lengths at THz frequencies are shorter than at GHz frequencies.[24,39] Therefore, IrAl bulk and IrAl/FM interface are accessed with different sensitivity by the two methods. Because composition ratios close to the IrAl/FM interface may differ from those in the bulk of IrAl, the two methods yield different results. We, thus, conducted XRD measurements to check the exact bulk composition of our samples (Fig. S8) and confirm them to be as nominally given throughout this study. Therefore, we interpret the shift of the global maximum at THz frequencies to originate from an altered composition at the IrAl/FM interface. At THz frequencies, we observe a second local maximum/plateau at a higher Al concentration, which is not present for the SCC efficiency at GHz frequencies.[10] As the exact interface structure may be quite different than the bulk, we do not attempt to link our THz measurements to crystalline textures or structural changes as done in Ref. 10. However, it is remarkable that the overall trend of the SCC efficiency in both frequency regimes is quite consistent even though the probed volume is significantly different.

In conclusion, we studied Ir_xAl_{1-x}|CoFeB thin-film bilayers with varying composition ratio x by THz emission spectroscopy. We

observe a strong dependence of the THz amplitude on x in agreement with previous DC studies. We infer that the spin-to-charge conversion efficiency in Ir_xAl_{1-x} amounts to 65% relative to Pt for $x = 0.48$ and rule out a possible dominant ISREE and orbital-to-charge conversion contributions. Our findings highlight IrAl alloys as a good candidate for SCC on ultrafast timescales, whose SCC efficiency could potentially be increased in further studies through FM/NM interface engineering,[18] optimization of the sample resistivity[40] or extend to ternary alloys.

See the supplementary material for details on THz emission and transmission raw data, linearly- and circularly polarized pump excitation, Fourier-transformed spectra of the time-domain THz signals, frequency-dependent impedances, charge-current sheet densities, and XRD data from IrAl|CoFeB.

AUTHOR DECLARATIONS
Conflict of Interest

Yes, T.S.S. and T.K. are shareholders of TeraSpinTec GmbH, and T.S.S. is an employee of TeraSpinTec GmbH. The authors have no conflicts to disclose.

Author Contributions

Junwei Tong: Data curation (equal); Formal analysis (lead); Investigation (lead); Methodology (equal); Visualization (equal); Writing – original draft (lead); Writing – review & editing (lead). **Peng Wang:** Formal analysis (supporting); Resources (lead); Writing – review & editing (supporting). **Hongsong Qiu:** Writing – review & editing (supporting). **Tom S. Seifert:** Writing – review & editing (supporting). **Ilya Kostanovski:** Formal analysis (supporting); Resources (supporting). **Stuart S. P. Parkin:** Funding acquisition (lead); Resources (lead); Supervision (equal); Writing – review & editing (supporting). **Tobias Kampfrath:** Conceptualization (equal); Funding acquisition (lead); Methodology (lead); Resources (lead); Supervision (equal); Writing – original draft (equal); Writing – review & editing (equal). **Oliver Gueckstock:** Conceptualization (equal); Data curation (equal); Formal analysis (supporting); Investigation (supporting); Methodology (lead); Supervision (equal); Validation (equal); Visualization (equal); Writing – original draft (lead); Writing – review & editing (lead).

DATA AVAILABILITY

The data that support the findings of this study are available from the corresponding author upon reasonable request.

REFERENCES

[1] J. Sinova, S. O. Valenzuela, J. Wunderlich et al., "Spin Hall effects," Rev. Mod. Phys. **87**, 1213–1260 (2015).

[2] S. Zhang and A. Fert, "Conversion between spin and charge currents with topological insulators," Phys. Rev. B **94**, 184423 (2016).

[3] S. D. Bader and S. S. P. Parkin, "Spintronics," Annu. Rev. Condens. Matter Phys. **1**, 71–88 (2010).

[4] C. Zhou, Y. Liu, Z. Wang et al., "Broadband terahertz generation via the interface inverse Rashba-Edelstein effect," Phys. Rev. Lett. **121**, 086801 (2018).

[5] H. Nakayama, Y. Kanno, H. An et al., "Rashba-Edelstein magnetoresistance in metallic heterostructures," Phys. Rev. Lett. **117**, 116602 (2016).

[6] S. D. Ganichev, E. Ivchenko, V. Bel'Kov et al., "Spin-galvanic effect," Nature **417**, 153–156 (2002).

[7] K. Kondou, R. Yoshimi, A. Tsukazaki et al., "Fermi-level-dependent charge-to-spin current conversion by Dirac surface states of topological insulators," Nat. Phys. **12**, 1027–1031 (2016).

[8] G.-Y. Guo, S. Murakami, T.-W. Chen et al., "Intrinsic spin Hall effect in platinum: First-principles calculations," Phys. Rev. Lett. **100**, 096401 (2008).

[9] C.-F. Pai, L. Liu, Y. Li et al., "Spin transfer torque devices utilizing the giant spin Hall effect of tungsten," Appl. Phys. Lett. **101**, 122404 (2012).

[10] P. Wang, A. Migliorini, S.-H. Yang et al., "Giant spin Hall effect and spin–orbit torques in 5d transition metal–aluminum alloys from extrinsic scattering," Adv. Mater. **34**, 2109406 (2022).

[11] E. Y. Vedmedenko, R. K. Kawakami, D. D. Sheka et al., "The 2020 magnetism roadmap," J. Phys. D **53**, 453001 (2020).

[12] T. Kampfrath, M. Battiato, P. Maldonado et al., "Terahertz spin current pulses controlled by magnetic heterostructures," Nat. Nanotechnol. **8**, 256–260 (2013).

[13] T. Seifert, S. Jaiswal, U. Martens et al., "Efficient metallic spintronic emitters of ultrabroadband terahertz radiation," Nat. Photonics **10**, 483–488 (2016).

[14] R. Rouzegar, L. Brandt, L. Nádvorník et al., "Laser-induced terahertz spin transport in magnetic nanostructures arises from the same force as ultrafast demagnetization," Phys. Rev. B **106**, 144427 (2022).

[15] P. Jiménez-Cavero, O. Gueckstock, L. Nádvorník et al., "Transition of laser-induced terahertz spin currents from torque- to conduction-electron-mediated transport," Phys. Rev. B **105**, 184408 (2022).

[16] G. Bierhance, A. Markou, O. Gueckstock et al., "Spin-voltage-driven efficient terahertz spin currents from the magnetic Weyl semimetals Co_2MnGa and Co_2MnAl," Appl. Phys. Lett. **120**, 082401 (2022).

[17] R. Rouzegar, A. L. Chekhov, Y. Behovits et al., "Broadband spintronic terahertz source with peak electric fields exceeding 1.5 MV/cm," Phys. Rev. Appl. **19**, 034018 (2023).

[18] O. Gueckstock, L. Nádvorník, M. Gradhand et al., "Terahertz spin-to-charge conversion by interfacial skew scattering in metallic bilayers," Adv. Mater. **33**, 2006281 (2021).

[19] M. Meinert, B. Gliniors, O. Gueckstock et al., "High-throughput techniques for measuring the spin Hall effect," Phys. Rev. Appl. **14**, 064011 (2020).

[20] R. Schneider, M. Fix, J. Bensmann et al., "Composition-dependent ultrafast THz emission of spintronic CoFe/Pt thin films," Appl. Phys. Lett. **120**, 042404 (2022).

[21] T. Huisman, R. Mikhaylovskiy, J. Costa et al., "Femtosecond control of electric currents in metallic ferromagnetic heterostructures," Nat. Nanotechnol. **11**, 455–458 (2016).

[22] P. Li, S. Liu, X. Chen et al., "Spintronic terahertz emission with manipulated polarization (STEMP)," Front. Optoelectron. **15**, 12 (2022).

[23] P. Borcherds, R. Hall, K. Kunc et al., "The lattice dynamics of gallium phosphide," J. Phys. C **12**, 4699 (1979).

[24] O. Gueckstock, R. L. Seeger, T. S. Seifert et al., "Impact of gigahertz and terahertz transport regimes on spin propagation and conversion in the antiferromagnet IrMn," Appl. Phys. Lett. **120**, 062408 (2022).

[25] Y.-H. Zhu, B. Hillebrands, and H. C. Schneider, "Signal propagation in time-dependent spin transport," Phys. Rev. B **78**, 054429 (2008).

[26] J. Jechumtál, R. Rouzegar, O. Gueckstock et al., "Accessing ultrafast spin-transport dynamics in copper using broadband terahertz spectroscopy," Phys. Rev. Lett. **132**, 226703 (2024).

[27] D. Gall, "Electron mean free path in elemental metals," J. Appl. Phys. **119**, 085101 (2016).

[28]D. Kong, X. Wu, B. Wang *et al.*, "Broadband spintronic terahertz emitter with magnetic-field manipulated polarizations," Adv. Opt. Mater. **7**, 1900487 (2019).

[29]T. Tanaka, H. Kontani, M. Naito *et al.*, "Intrinsic spin Hall effect and orbital Hall effect in 4*d* and 5*d* transition metals," Phys. Rev. B **77**, 165117 (2008).

[30]H. Kontani, T. Tanaka, D. Hirashima *et al.*, "Giant orbital Hall effect in transition metals: Origin of large spin and anomalous Hall effects," Phys. Rev. Lett. **102**, 016601 (2009).

[31]D. Go, D. Jo, C. Kim *et al.*, "Intrinsic spin and orbital Hall effects from orbital texture," Phys. Rev. Lett. **121**, 086602 (2018).

[32]T. S. Seifert, D. Go, H. Hayashi *et al.*, "Time-domain observation of ballistic orbital-angular-momentum currents with giant relaxation length in tungsten," Nat. Nanotechnol. **18**, 1132–1138 (2023).

[33]Y. Xu, F. Zhang, A. Fert *et al.*, "Orbitronics: Light-induced orbital currents in Ni studied by terahertz emission experiments," Nat. Commun. **15**, 2043 (2024).

[34]S. Kumar and S. Kumar, "Ultrafast THz probing of nonlocal orbital current in transverse multilayer metallic heterostructures," Nat. Commun. **14**, 8185 (2023).

[35]P. Wang, Z. Feng, Y. Yang *et al.*, "Inverse orbital Hall effect and orbitronic terahertz emission observed in the materials with weak spin-orbit coupling," npj Quantum Mater. **8**, 28 (2023).

[36]R. Xu, X. Ning, H. Cheng *et al.*, "Terahertz generation via the inverse orbital Rashba-Edelstein effect at the Ni/CuOx interface," Phys. Rev. Res. **7**, L012042 (2025).

[37]Y. Liu, Y. Xu, A. Fert *et al.*, "Efficient orbitronic terahertz emission based on CoPt alloy," Adv. Mater. **36**, 2404174 (2024).

[38]G. Li, R. Medapalli, R. V. Mikhaylovskiy *et al.*, "THz emission from Co/Pt bilayers with varied roughness, crystal structure, and interface intermixing," Phys. Rev. Mater. **3**, 084415 (2019).

[39]T. S. Seifert, N. M. Tran, O. Gueckstock, S. M. Rouzegar, L. Nadvornik, S. Jaiswal, G. Jakob, V. V. Temnov, M. Münzenberg, M. Wolf, M. Kläui, and T. Kampfrath, "Terahertz spectroscopy for all-optical spintronic characterization of the spin-Hall-effect metals Pt, W and Cu$_{80}$Ir$_{20}$," J. Phys. D: Appl. Phys. **51**(36), 364003 (2018).

[40]F. Janus, N. Beermann, J. Yadav *et al.*, "Enhanced THz emission from spintronic emitters with Pt-Al alloys," arXiv:2504.07614 (2025).